

Journal of Materials Chemistry A

Accepted Manuscript



This is an *Accepted Manuscript*, which has been through the Royal Society of Chemistry peer review process and has been accepted for publication.

Accepted Manuscripts are published online shortly after acceptance, before technical editing, formatting and proof reading. Using this free service, authors can make their results available to the community, in citable form, before we publish the edited article. We will replace this *Accepted Manuscript* with the edited and formatted *Advance Article* as soon as it is available.

You can find more information about *Accepted Manuscripts* in the [Information for Authors](#).

Please note that technical editing may introduce minor changes to the text and/or graphics, which may alter content. The journal's standard [Terms & Conditions](#) and the [Ethical guidelines](#) still apply. In no event shall the Royal Society of Chemistry be held responsible for any errors or omissions in this *Accepted Manuscript* or any consequences arising from the use of any information it contains.

Thienoisindigo (TIIG)-Based Small Molecules for Understanding of Structure–Property–Device Performance Correlations

Cite this: DOI: 10.1039/x0xx00000x

Hyojin Kang,[‡] Su Yeon An,[‡] Bright Walker, Seyeong Song, Taehyo Kim, Jin Young Kim, and Changduk Yang

Received 00th January 2012,
Accepted 00th January 2012

DOI: 10.1039/x0xx00000x

www.rsc.org/

In this contribution, a series of small molecule semiconductors based on the recently conceived thienoisindigo (TIIG) and three different end-capping moieties (benzene (Bz), naphthalene (Np), and benzofuran (Bf)) with varied electron-donating strength and conformations has been synthesized by Suzuki coupling and utilized for organic photovoltaics (OPVs). Incorporation of different end-capping blocks onto the TIIG core facilitated the tuning of optical properties and the electronic structure (HOMO/LUMO energy levels), solid-state morphology and performance in OPVs. It is apparent that the bandgaps within this series (**TIIG-Bz**, **TIIG-Np**, and **TIIG-Bf**) were progressively red-shifted and the absorption coefficients were enhanced by increasing the conjugation length and/or the donor ability of the end-capping units. In addition, HOMO and LUMO levels were shown to simultaneously follow changes made to the end-capping moieties. The best performing OPVs using **TIIG-Np**:PC₇₁BM exhibited a power conversion efficiency (PCE) of 1.81% with $J_{sc} = 7.15 \text{ mA cm}^{-2}$, $FF = 0.39$, and $V_{oc} = 0.66 \text{ V}$. With the aim of exploring underlying structure-property relationships for this new class of molecular systems, we have quantitatively investigated various morphological structures in both the pristine small molecule films and small molecule/PC₇₁BM blend films using a combination of grazing incidence wide angle X-ray scattering (GIWAXS) and atomic force microscopy (AFM). In this study, a correlation between the molecular structure, thin film morphology, and photovoltaic properties of these conjugated small molecules was established that provides guidance for the molecular design of new photovoltaic semiconductors based on TIIG units.

Introduction

Bulk heterojunction (BHJ) organic photovoltaics (OPVs) based on conjugated semiconductors as electron-donor materials blended with fullerene derivatives as electron-acceptor materials are a promising technology to low-cost, light-weight, flexible, large-area, and energy-generation applications.^{1–4} Due to their desirable film-forming capability and mechanical robustness, polymeric donor materials have constituted the majority of research relating to BHJ OPVs.^{5, 6} Consequently, through a combination of polymer design, morphology control, structural insight, and device engineering, OPVs based on polymer/fullerene blends have reached significant milestones with over 10% power conversion efficiencies (PCEs).^{7–9} Nonetheless, polymeric donors suffer from inherent disadvantages such as batch-to-batch variations, chain-end contamination, broad molecular-weight distributions and difficult purification methods, which can preclude further

improvement of overall device performance and device consistency.^{10–12} In contrast, small molecules—which possess not only well-defined structures with a mono-disperse nature but also negligible batch-to-batch variation—have significantly received attention as alternatives to polymeric counterparts.¹³ Therefore, it is true that more reproducible fabrication protocols and a better understanding of molecular structure–property relationships are anticipated in small molecule BHJ systems. In order to efficiently improve PCEs, the donor materials, in principle, require wide absorption within the solar spectrum, suitable energy levels, high charge-carrier mobilities and good charge transport pathways to the electrodes.

Taking into account the above issues, one of the most promising classes of semiconductors is bislactam motifs including diketopyrrolopyrrole (DPP), benzodipyrrolidone (BDP), isoindigo (IIG), and thienoisindigo (TIIG), which have shown some of the highest PCEs^{14, 15} reported to date and have

been used to fabricate transistor devices with unprecedented Among such high-performance pigments, the recently conceived TIIG moiety exhibits superior co-planarity *via* S...O interactions and improved electronic delocalization *via* a quinoidal structure along the backbone, leading to high absorption coefficients, broad light absorption and high charge carrier mobilities.¹⁹⁻²² We previously reported a series of TIIG-containing ultralow-bandgap polymers, showing excellent charge transport properties.^{17, 22} Despite the promising performance of TIIG-based polymers in transistor devices, much less work has appeared on the use of TIIG units in BHJ OPVs, which has included the TIIG-based small molecule incorporating the benzofuran unit.²³⁻²⁵

Here we present a synthesis of three low-bandgap TIIG-based small molecules (**TIIG-Bz**, **TIIG-Np**, and **TIIG-Bf**) in which a TIIG core was coupled with benzene (Bz), naphthalene (Np), or benzofuran (Bf) moieties, respectively. With the goal of establishing how structural variations influence optical properties, energy levels, morphology, molecular packing, charge transport, and OPV performance, this new class of TIIG-based materials was investigated thoroughly. Our in-depth study provides a relevant step forward to understanding structure-property relationships of the TIIG family.

Results and Discussion

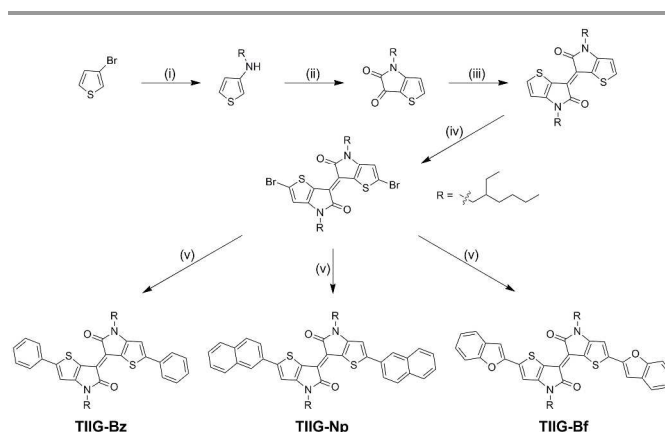
Synthesis and Characterization

The synthetic routes to TIIG monomer and the target small molecules (**TIIG-Bz**, **TIIG-Np**, and **TIIG-Bf**) in which TIIG incorporates with benzene (Bz), naphthalene (Np), or benzofuran (Bf) are outlined in Scheme 1. First, TIIG monomer, (*E*)-2,2'-dibromo-4,4'-bis(2-ethylhexyl)-[6,6'-bithieno[3,2-*b*]pyrrolylidene]-5,5'-(4*H*,4*H'*)-dione was synthesized as previously reported.²⁰ The 2-Ethylhexyl alkyl chain was introduced onto the TIIG core to ensure solubility. The three small molecules were then obtained through palladium-catalyzed Suzuki coupling in degassed toluene/water to append phenylboronic acid, naphthalene-2-boronic acid pinacol ester, or benzo[*b*]furan-2-boronic acid, as end-capping building blocks, respectively, using tris(dibenzylideneacetone)dipalladium (0) as a catalyst, tri(*o*-tolyl)phosphine as a ligand, and potassium phosphate tribasic as a base. The detailed synthetic procedures are described in the Experimental section.

Optical and Electrochemical Properties as well as Theoretical Calculations

The UV-Vis absorption spectra of the three small molecules **TIIG-Bz**, **TIIG-Np**, and **TIIG-Bf** both in chloroform solution and as thin films are shown in Fig.1, while the photophysical data are summarized in Table 1.

mobilities.¹⁶⁻¹⁸



Scheme 1. Synthetic routes to TIIG monomer and TIIG-based small molecules used for OPVs. Reagents and conditions: (i) 2-Ethylhexyl-1-amine, Cu, CuI, K₃PO₄, 2-(dimethylamino)ethanol, 80 °C, 72 h, 40%; (ii) Oxalyl chloride, triethylamine, DCM, rt, overnight, 28%; (iii) Lawesson's reagent, *o*-xylene, 60 °C, 19%; (iv) NBS, THF, rt, 78%; (v) Phenylboronic acid, naphthalene-2-boronic acid pinacol ester, or benzo[*b*]furan-2-boronic acid, Pd₂(dba)₃, P(*o*-tolyl)₃, K₃PO₄ aqueous solution, aliquat 336, toluene, 90 °C, 48 h for **TIIG-Bz**, 80%; for **TIIG-Np**, 78%; for **TIIG-Bf**, 75.6%.

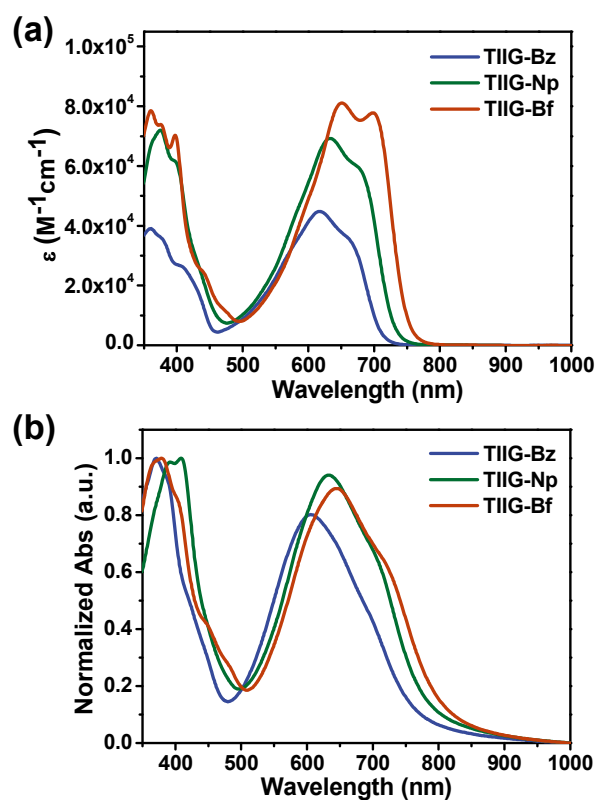


Fig. 1. UV-Vis absorption spectra of TIIG-based small molecules in (a) CHCl₃ solution (2.72×10^{-5} M for **TIIG-Bz**, 1.57×10^{-5} M for **TIIG-Np**, and 1.62×10^{-5} M for **TIIG-Bf**) and (b) as thin films (10 mg mL⁻¹, 800 rpm, 60 s).

All the three small molecules featured dual-band absorptions both in solution and as thin films: a sharp one in the range of 350–450 nm, which can be assigned to localized π – π^* transitions, and another broader one with a vibronic shoulder in the range of 500–900 nm, which accounts for intra-molecular

charge transfer (ICT) ascribed to the interplay of the donor–acceptor architecture. In solution (Fig. 1a), the absorption profiles of **TIIG-Np** and **TIIG-Bf** showed more vibronic fine structure than that of **TIIG-Bz**, potentially due to a better co-planarity induced by the ring-fused end-capping blocks with the extended conjugated length. Additionally, it is apparent that the absorption coefficients of the ICT bands increased in the order of **TIIG-Bf**>**TIIG-Np**>**TIIG-Bz**, which would indicate that the strength of the electron donating abilities of the end-capping blocks influence the oscillator strength of the molecule.

Very interestingly, compared to their corresponding solution spectra, the film absorption spectra (Fig. 1b) showed red shifts in the absorption onsets (λ_{onset}), whereas slight blue shifts in their absorption maxima (λ_{max}) were observed. In addition, the relative intensities of ICT bands in the films were consistent with the trend observed in the solution absorption coefficients. Although the reason for the blue shifts of λ_{max} remains unclear at the current stage, it is clear that both **TIIG-Bf** and **TIIG-Np** showed relatively high absorption coefficient values and spectral broadening compared to **TIIG-Bz**, which is beneficial for efficient photon harvesting. Similar phenomena have previously been reported by Li and coworkers, where extending π -bridges from thiophene to bithiophene was found to increase the absorption coefficients of the molecules.²⁶ Optical bandgaps ($E_{\text{g}}^{\text{opt}}$) estimated from the absorption onset of the films are 1.62, 1.58, and 1.54 eV for **TIIG-Bz**, **TIIG-Np**, and **TIIG-Bf**, respectively, being consistent with the trend of the above coefficient results.

Cyclic voltammetry (CV) of the small molecules in dichloromethane solution was used to probe their frontier electronic energy levels (Fig. 2a). The relevant electrochemical data are compiled in Table 1. All the small molecules revealed a reversible reduction and two reversible oxidations with similar intensities. For a single molecule with electron-accepting (TIIG) and electron-donating units, one might expect that by changing electron-donating blocks, only the lowest unoccupied molecular orbital (LUMO) would be affected.

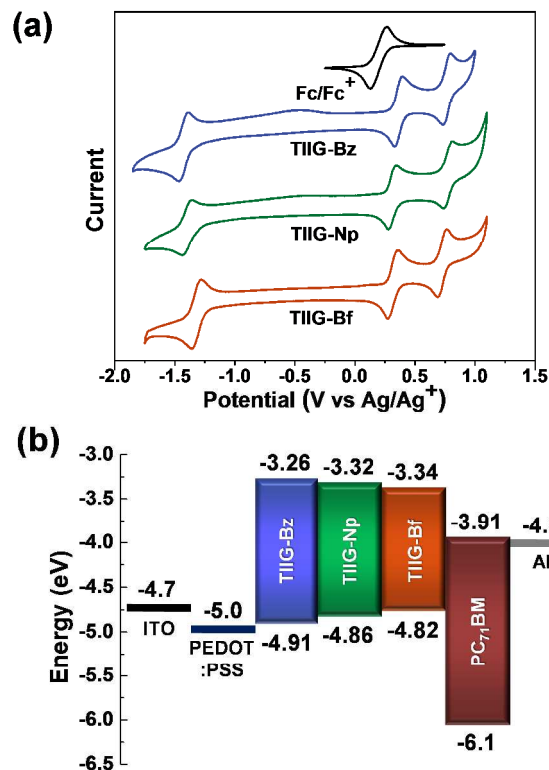


Fig. 2. (a) Cyclic voltammograms of TIIG-based small molecules in CH_2Cl_2 solution. (b) Energy level diagrams of the components of BHJ devices in this study.

However, Fig. 2a clearly shows that the electron-donating end groups in the TIIG-based materials can have an equally large effect on the highest occupied molecular orbital (HOMO) level of the small molecules as on the LUMO level.

In going from Bf to Np and Bz end-capping blocks, a systematic lowering of the HOMO level was observed. This observation reflects that empirical electron-donating qualities of end-capping groups are manifested in the sequence of $\text{Bz} < \text{Np} < \text{Bf}$, which is also in agreement with the aforementioned trend based on theoretical profiles. Overall, our TIIG-based molecules exhibited higher HOMO levels compared to the IIG-based analogs^{27, 28} due to the enhanced charge delocalization *via* a quinoidal structure of the TIIG backbone.²⁰

Table 1. Photophysical and electrochemical properties of TIIG-based small molecules as derived from UV-Vis absorption spectra and cyclic voltammetry curves.

	$\lambda_{\text{max}}^{\text{solution}}$ (nm)	$\lambda_{\text{max}}^{\text{film}}$ (nm)	$\lambda_{\text{edge}}^{\text{film}}$ (nm)	$E_{\text{g}}^{\text{opt}}$ (eV) ^a	E_{HOMO} (eV) ^b	E_{LUMO} (eV) ^b	$E_{\text{g}}^{\text{elec}}$ (eV) ^c
TIIG-Bz	361, 617	371, 605	764	1.62	-4.91	-3.26	1.65
TIIG-Np	375, 633	409, 633	782	1.58	-4.86	-3.32	1.54
TIIG-Bf	360, 651, 698	378, 644	804	1.54	-4.82	-3.34	1.48

^aCalculated from the absorption band edges of the small molecule films, $E_{\text{g}}^{\text{opt}} = 1240/\lambda_{\text{edge}}^{\text{film}}$

^bSolution in 0.1 M $\text{CH}_2\text{Cl}_2/n\text{-Bu}_4\text{NPF}_6$, versus ferrocene/ferrocenium at 100 mVs^{-1} . HOMO and LUMO estimated from the onset oxidation and reduction potentials, respectively, assuming the absolute energy level of ferrocene/ferrocenium to be 4.8 eV below vacuum.

$${}^cE_g^{\text{elec}} (\text{eV}) = E_{\text{LUMO}} - E_{\text{HOMO}}$$

In contrast, the LUMO levels of three compounds were as follows: -3.34 eV for **TIIG-Bf**, -3.32 eV for **TIIG-Np**, and -3.26 eV for **TIIG-Bz**, being opposite to the sequence of HOMO levels above.

The electrochemical gap (E_g^{elec}) defined as $E_g^{\text{elec}} (\text{eV}) = E_{\text{LUMO}} - E_{\text{HOMO}}$ followed the same trend as the E_g^{opt} above, but was consistently somewhat larger by $\Delta E = 0.03$ – 0.06 eV. Such a small difference is not unexpected because electrons are extracted or added in the determination of E_{ox} and E_{red} , whereas the optical gap provides the energetic difference for an intramolecular excitonic state, with the hole and the electron energies stabilized by Coulomb attraction.²⁹ From the CV results, the three molecules are found to have moderate frontier energy levels that are appropriately aligned with those of PC₇₁BM (Fig. 2b).

Density functional theory (DFT) calculations (B3LYP/6-31G) were carried out to gain additional insights into the theoretical electronic features, depending on the different molecular structures of the donor units (Fig. 3). The optimized molecular orbital distributions reveal that the HOMOs are mostly distributed along the whole conjugated backbones while the LUMOs are partially localized on TIIG core in all cases. This implies that the three small molecules have *p*-type properties in common.

It is interesting to point out that altering the electron-donating units from Bz to Np and Bf gives rise to a successive narrowing of dihedral angles between TIIG core and the end-capping blocks, with Bf affording the smallest value of 0.14°.

OPVs Performance

Photovoltaic applications of **TIIG-Bz**, **TIIG-Np**, and **TIIG-Bf** were investigated in solar cell devices with the device configura-

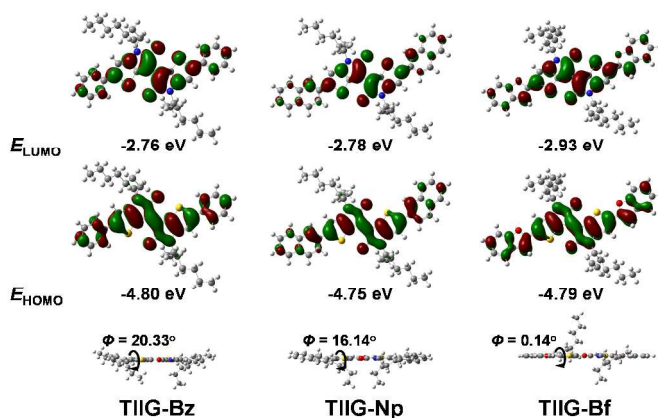


Fig. 3. Optimized frontier molecular orbitals and geometries for TIIG-based small molecules simulated *via* density functional theory (DFT) calculations (B3LYP/6-31G).

tion glass/ITO/PEDOT:PSS/small molecule:PC₆₁BM or PC₇₁BM/Al. Initially, the ratios (w/w) between the small molecules and PC₆₁BM were varied from 3:7 to 7:3 in order to identify suitable donor:acceptor ratios for this system.

The photovoltaic parameters of these devices are reported in Table S1. PC₆₁BM was replaced with PC₇₁BM using optimized device fabrication parameters and slightly enhanced results were obtained. The fabrication conditions were further explored by changing concentrations, spin-coating rates, and using solvent additives. Among all of these conditions, optimal performance was observed using blend solutions in chloroform with donor:acceptor ratios of 7:3, 6:4, and 6:4 for **TIIG-Bz**, **TIIG-Np**, and **TIIG-Bf**, respectively. These devices showed dramatically improved characteristics after thermal annealing at 100 °C.

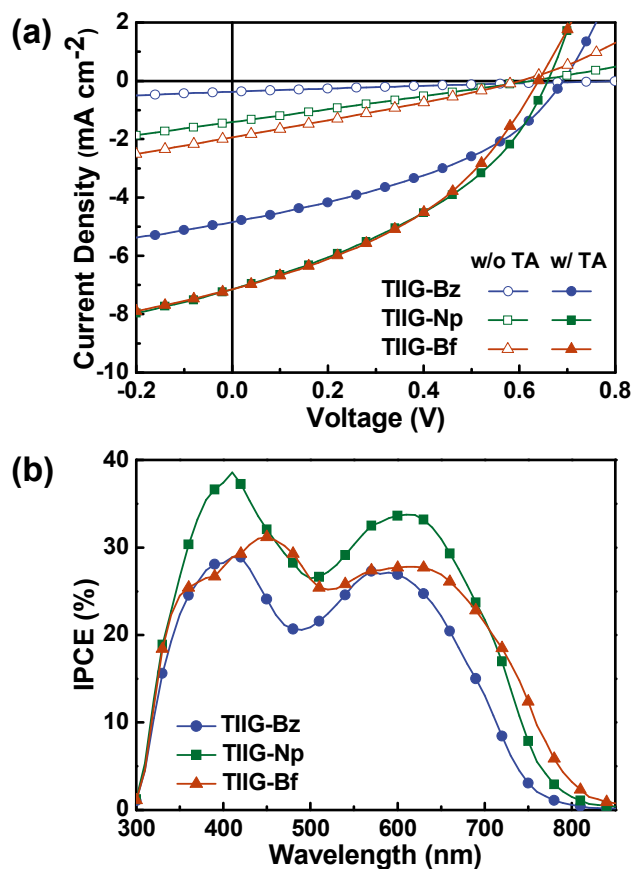


Fig. 4. (a) Current density–voltage (J – V) characteristics without (w/o TA) and with (w/ TA) thermal annealing at 100 °C. (b) Incident photon-to-current efficiency (IPCE) results of conventional structures for **TIIG-Bz**:PC₇₁BM (7:3 (w/w)), **TIIG-Np**:PC₇₁BM (6:4 (w/w)), and **TIIG-Bf**:PC₇₁BM (6:4 (w/w)) after thermal annealing at 100 °C, respectively.

Table 2. Summary of photovoltaic device characteristics of TIIG-based small molecules.

Active Layer	Annealing Temp. (°C)	J_{sc} (mA cm ⁻²)	V_{oc} (V)	FF	PCE (%)
TIIG-Bz :PC ₇₁ BM	w/o	0.37	0.82	0.22	0.07
	100	4.85	0.69	0.39	1.32
TIIG-Np :PC ₇₁ BM	w/o	1.41	0.63	0.25	0.22
	100	7.15	0.66	0.39	1.81
TIIG-Bf :PC ₇₁ BM	w/o	1.83	0.61	0.28	0.31
	100	7.15	0.64	0.39	1.80

Fig. 4a displays the current density–voltage (J – V) characteristics of OPVs based on **TIIG-Bz**, **TIIG-Np**, and **TIIG-Bf**, respectively, under AM 1.5 G calibrated solar simulator with an irradiation intensity of 100 mW cm⁻². A summary of the device parameters can be found in Table 2.

As-cast devices of all the three small molecules exhibited very low power conversion efficiencies (PCEs) of about 0.07–0.31%. However, an increase in FF s (to 0.39 in all cases) coupled with a dramatic increase in J_{sc} s to 4.85, 7.15, and 7.15 mA cm⁻², for **TIIG-Bz**, **TIIG-Np**, and **TIIG-Bf**, respectively, was evident after thermal annealing (Fig. 4a). The V_{oc} s were concomitantly changed by -0.13, 0.03, and 0.03 V for **TIIG-Bz**, **TIIG-Np**, and **TIIG-Bf**, respectively. Thermal annealing at 100 °C thus increased the PCEs to 1.32, 1.81, and 1.80% for **TIIG-Bz**, **TIIG-Np**, and **TIIG-Bf**, respectively.

To investigate the spectral photocurrent response of the devices, incident photon-to-current efficiency (IPCE) spectra were collected. As shown in Fig. 4b, all the three small molecules exhibited IPCE contributions throughout the visible spectrum. The IPCE spectra exhibited two major peaks in the ranges of 400–450 nm and 570–620 nm for these small molecules, which match the absorption bands of the blends observed in UV-Vis spectra. **TIIG-Np** showed the highest photon conversion efficiency with a maximum of 37% near 400 nm and an onset near 775 nm. **TIIG-Bf** covered the greatest spectral range (up to 800 nm) with a maximum of 31% at 450 nm, while **TIIG-Bz** covered the narrowest (up to 750 nm) with the lowest overall efficiency including a maximum of 29% near 400 nm, consistent with the relatively low J_{sc} produced by this material.

In order to investigate the charge transport behavior in BHJ blends with PC₇₁BM, electron and hole mobilities (μ_e and μ_h , respectively) were measured using the space charge limited current (SCLC) technique.³⁰ Detailed device fabrication and measurement procedures are reported in the experimental section. The J – V curves of electron and hole-only diodes are plotted in Fig. S1 while μ_e and μ_h data are reported in Table S2. **TIIG-Bz** exhibited a modest electron mobility of 3.11×10^{-4} cm² V⁻¹s⁻¹ and rather low hole mobility of 5.5×10^{-6} cm² V⁻¹s⁻¹. **TIIG-Np** exhibited balanced, but low μ_e and μ_h values of 4.10×10^{-5} and 2.02×10^{-5} cm² V⁻¹s⁻¹, respectively, while **TIIG-Bf**

exhibited the highest μ_e and μ_h values of 1.00×10^{-3} and 2.19×10^{-4} cm² V⁻¹s⁻¹ respectively. A combination of relatively low μ_h and mis-matched μ_e/μ_h ratios may explain the low observed FF s in all three materials and may also be a factor which limits the J_{sc} of **TIIG-Bz**-based photovoltaic device.³⁰

Thin-Film Microstructure Analyses

For more detailed understanding of the photovoltaic trends and morphology of pristine small molecules and blends with PC₇₁BM films before and after annealing, molecular spacing and packing orientation relative to the substrate were analyzed by grazing incidence wide angle X-ray scattering (GIWAXS) and atomic force microscopy (AFM). Fig. 5 shows GIWAXS images of pristine small molecules and small molecule:PC₇₁BM blend films deposited from chloroform before and after thermal annealing. Detailed GIWAXS profiles are plotted and shown in Fig. 6 and Table S3.

GIWAXS patterns for pristine films of all three TIIG materials are shown in Fig. 5a–c with corresponding horizontal and vertical line cuts in Fig. 6. Diffraction peaks corresponding to both lamellar packing and π – π stacking were observed in both in-plane and out-of-plane directions for all pristine small molecule films; lamellar peaks (100) were stronger in the q_z (out of plane) direction while π – π stacking peaks (010) were stronger in the q_{xy} direction for this series of molecules. This implies that the pristine small molecules preferentially self-assembled into an edge-on orientation when spin-coated onto the substrates. **TIIG-Bz** displayed significant lamellar packing with clear peaks corresponding to lamellar (100), (200) diffraction planes and a π – π stacking plane (010) in the out-of-plane direction. A series of 4 weaker peaks were also apparent in the out-of-plane direction in the range of $q_z = 0.9$ – 1.4 Å⁻¹. Like **TIIG-Bz**, **TIIG-Np** also showed several strong diffraction peaks, with four clear lamellar peaks in the out of plane direction. These peaks may correspond to (100), (200), (300) lamellar diffraction planes and a (010) π – π stacking plane. Peaks corresponding to (100), (300), and (010) diffraction planes were also apparent in the in-plane direction for **TIIG-Np**. **TIIG-Bf** exhibited the weakest lamellar packing with only a (100) peak apparent in the in-plane direction. It is noteworthy that pristine **TIIG-Np** and **TIIG-Bz** films showed higher crystallinity, in terms of number and sharpness of diffraction peaks, than **TIIG-Bf**, even though **TIIG-Bf** molecule has the most planar structure (with the smallest dihedral angle as indicated by DFT calculations) and should undergo π – π stacking the most easily. However, the relatively low crystallinity of **TIIG-Bf** is consistent with previous observed tendencies for the Bf end-capping group.³¹

GIWAXS patterns and line-cut properties for each small molecule:PC₇₁BM blend film are shown in Fig. 5d–f and Fig. 6. All three small molecule BHJ films exhibited only lamellar packing arising from the (100) plane with a complete disappearance of the π – π interaction peak. The alkyl side chains of the small molecules were thus still able to self-assemble into a lamellar structure in the presence of PCBM, as evidenced by a

broad lamellar (100) peak. However, the presence of PC₇₁BM molecules appears to have disrupted the intermolecular π - π

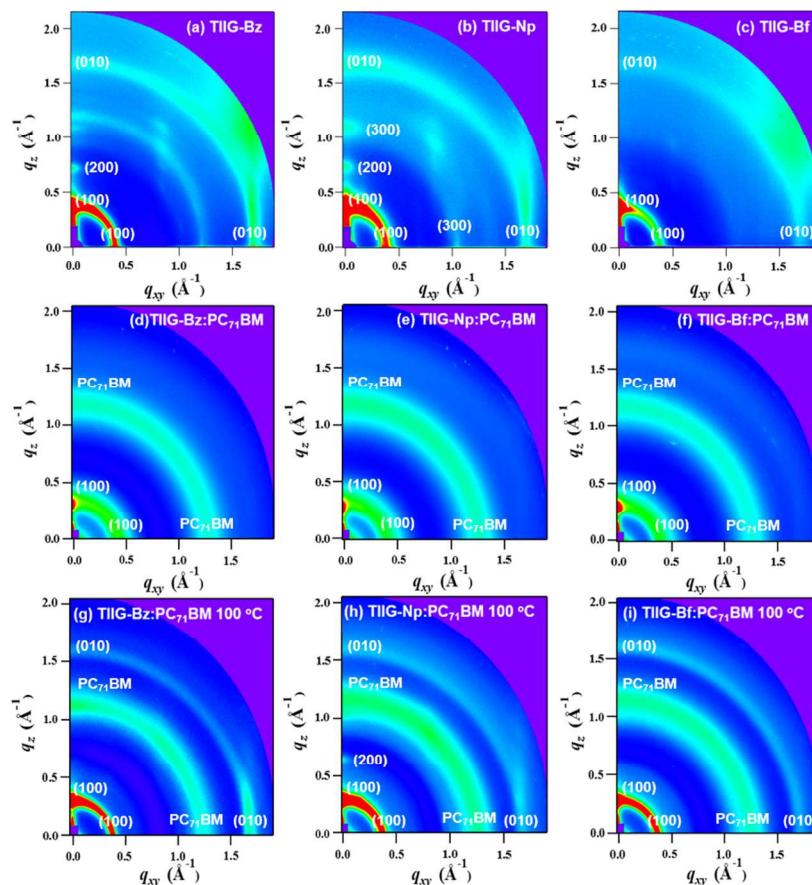


Fig. 5. GIWAXS images of (a–c) pristine small molecule films, small molecule:PC₇₁BM blend films (d–f) without and (g–i) with thermal annealing at 100 °C. Left, middle, and right columns show images corresponding to **TIIG-Bz**, **TIIG-Np**, and **TIIG-Bf**, respectively.

interactions compared to the pristine condition as the (010) peak disappeared completely for all three materials.³² These results are consistent with observations of the film morphology, in which AFM images show that all three molecules formed amorphous, smooth films upon blending with PC₇₁BM, including RMS roughness values of less than 0.5 nm.

After thermal annealing (Fig. 5g–i, Fig. 6 and Table S3), the thermal motion of the molecules at 100 °C enabled them to self-assemble into crystalline domains as evidenced by the re-appearance of diffraction peaks in all of the blend films. The **TIIG-Bz** blend showed the appearance of a (010) π - π interaction peak and sharpening of the (100) lamellar peak in both q_z and q_{xy} directions upon thermal annealing. As in the case of the pristine films, the intensity of the (010) peak was greater in the in-plane direction while the lamellar (100) peak was more intense in the out-of-plane direction, consistent with a tendency of the material to undergo edge-on packing on the substrate and consistent with observations of the pristine film. The annealed **TIIG-Np**:PC₇₁BM blend exhibited well-resolved diffraction patterns including strong (010) peaks in both the in-plane and out-of-plane directions, corresponding to π - π interactions, as well as (100) and (200) lamellar peaks in the out-of-plane direction (Fig. 5h, Fig. 6 and Table S3). As with

TIIG-Bz, the intensity of the diffraction peaks corresponding to lamellar packing ((100) and (200) planes) were again sharper and more intense in the out-of-plane direction, consistent with the pristine films, reflecting a tendency of this material to undergo edge-on packing on the substrate. The annealed **TIIG-Bf** blend showed similar tendency as annealed **TIIG-Bz** including the appearance of a (010) π - π interaction peak and sharpening of the (100) lamellar peak upon thermal annealing. As observed in the pristine films, **TIIG-Bf** appeared to have the lowest crystallinity, although the (010) π - π interaction peak was recovered and the (100) lamellar peak became sharper upon thermal annealing, the peaks were broader than the **TIIG-Bz** material.

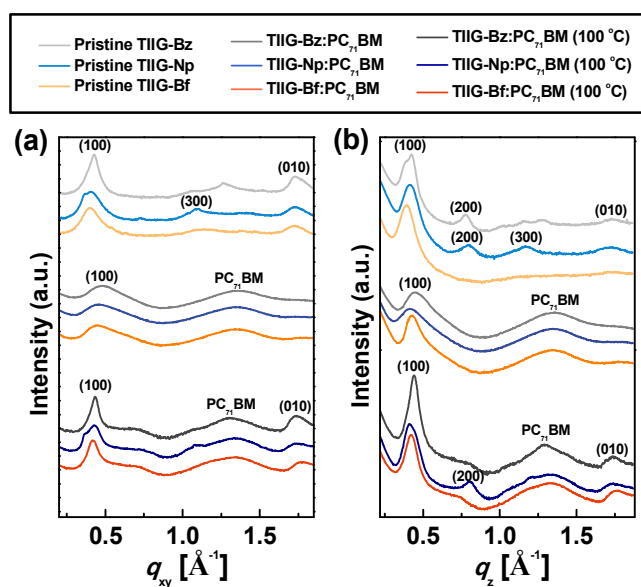


Fig. 6. Scattering line-cuts along (a) in-plane and (b) out-of-plane direction for pristine small molecules, small molecule:PC₇₁BM blend films without and with thermal annealing at 100 °C.

In order to probe surface morphology, tapping-mode AFM images were collected for pristine films of each molecule, as well as for as-cast and annealed BHJ films with PC₇₁BM. Height images are reported in Fig. 7 while the corresponding phase images are reported in Fig. S2. **TIIG-Bz** and **TIIG-Np** films exhibited bumpy and aggregated surface features with an RMS roughness' of 0.642 nm and 4.09 nm, respectively, while **TIIG-Bf** did not show clear structural features and had the lowest RMS roughness (0.373 nm). The lack of observable aggregate features in the pristine **TIIG-Bf** film is consistent with the observation that this molecule also exhibited the weakest GIWAXS pattern as a pristine film.

AFM images of as-cast BHJ films are reported in Fig. 7d–f, and all show smooth amorphous surfaces with RMS roughness' of 0.263, 0.459, and 0.407 nm for **TIIG-Bz**, **TIIG-Np**, and **TIIG-Bf**, respectively, consistent with the relatively weak diffraction patterns observed for as-cast films of each molecule. The surface morphologies of annealed BHJ films (Fig. 7g–i) did not clearly follow the GIWAXS results; in the annealed films, **TIIG-Bf**, showed the roughest films with an RMS roughness of 1.11 nm, while **TIIG-Np** showed intermediate roughness (0.729 nm) and the **TIIG-Bz** blend was the smoothest (0.528 nm).

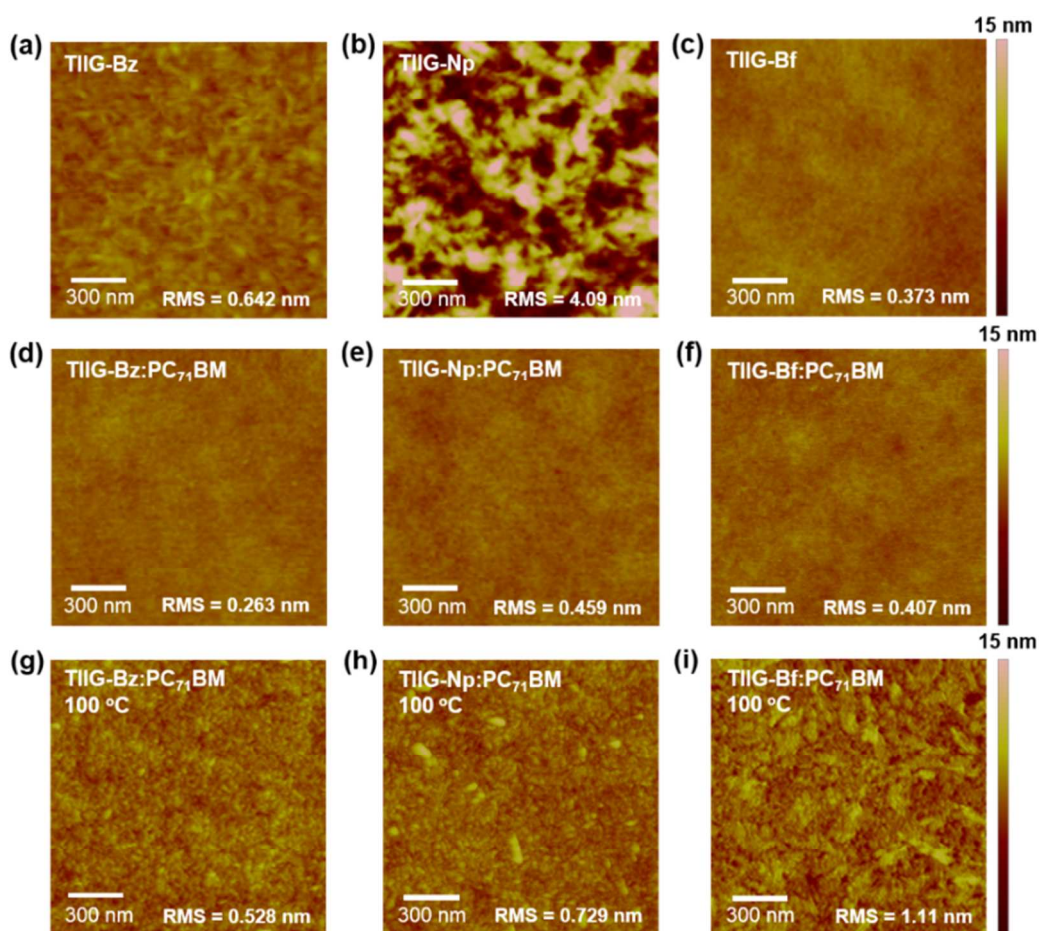


Fig. 7. AFM topography height images of (a–c) pristine small molecules, small molecule:PC₇₁BM blend films (d–f) without and (g–i) with thermal annealing at 100 °C. Left, middle, and right columns show images corresponding to **TIIG-Bz**, **TIIG-Np**, and **TIIG-Bf**, respectively. Each film was prepared on glass/ITO/PEDOT:PSS substrates. The size of all images is 1.5 μm × 1.5 μm.

ARTICLE

nm). These differences in roughness may be due to different degrees of phase separation in each material or different thermal transition temperatures. These physical characteristics of the films before and after thermal annealing provide useful information about the crystallinity, crystal formation and internetworking of donor and acceptor materials in the blend system; these film attributes are strongly correlated with the OPV device behavior.³³ All three blended small molecules displayed more obvious and stronger lamellar packing and π - π stacking after thermal annealing at 100 °C. In AFM images, the RMS roughness of three small molecules increased upon thermal annealing; similar tendencies have been observed in the isoindigo-based oligothiophene films.²⁸ From this information, we presume that thermal motion upon annealing allows crystallization of the donor phase while allowing phase separation to occur between the donor and PC₇₁BM phases.¹² These changes in material structure allow enhanced charge transport through the active layer, improving J_{sc} and FF .³³ These observations are consistent with the dramatic increase in J_{sc} s in the photovoltaic devices after thermal annealing for all three materials. The increase in J_{sc} s occurred concomitantly with a dramatic increase in PCEs to 1.32, 1.81, and 1.80% for **TIIG-Bz**, **TIIG-Np**, and **TIIG-Bf** respectively. Although it is difficult to precisely identify the cause for the lower J_{sc} and PCE in **TIIG-Bz**, the low μ_h and unbalanced carrier mobilities point to difficulties in charge carrier extraction with this material.

Conclusions

In summary, small molecules (**TIIG-Bz**, **TIIG-Np**, and **TIIG-Bf**) using the recently conceived electron-accepting TIIG unit and three different electron-donating end-capping blocks (Bz, Np, and Bf) have been synthesized, characterized, and used in BHJ OPVs as donor materials, in order to establish a useful platform to understand structure-property correlations in TIIG-based small molecule semiconductors. Together with theoretical calculations, the optical absorption and electrochemical potentials were used to determine their intrinsic optophysical properties and the electronic structure (HOMO/LUMO energy levels). Red shifts in λ_{max} as well as the absorption intensities of the ICT bands were directly proportional to the strength of end-capping donor moieties (Bz < Np < Bf) in small molecules. Both the HOMO and LUMO levels could be tuned as the end-capping moieties were varied. Within this series, the best solar cell devices based on a **TIIG-Np**:PC₇₁BM blend gave $J_{sc} = 7.15 \text{ mA cm}^{-2}$, $FF = 0.39$, and $V_{oc} = 0.66 \text{ V}$, resulting in a PCE as high as 1.81%. Detailed analysis of GIWAXS and AFM results was used to quantify not

only the morphology behavior of pristine small molecule films but also the structural changes occurring in small molecule/PC₇₁BM blends during thermal annealing at 100 °C in terms of the donor molecule lamellar orientation spread, backbone spacing along the alkyl-stacking direction, domain sizes, crystalline disorder, and the relative distribution of PC₇₁BM aggregates in the BHJ active layer. This work demonstrates that TIIG-based small molecule semiconductors have efficient light harvesting capabilities, suitable energy levels, and self-organized nanostructures suitable for use in BHJ OPVs. We believe that with more fine-tuning of TIIG-based materials, combined with optimized device processing methods, BHJ OPVs with high efficiencies are possible.

Experimental Section

Materials and Instruments

All chemicals and reagents were purchased from Sigma-Aldrich, Alfa Aesar Chemical Company, and Tokyo Chemical Industry Co., Ltd. and used without any further purification. All solvents were ACS and anhydrous grade by distillation. (*E*)-2,2'-Dibromo-4,4'-bis(2-ethylhexyl)-[6,6'-bithieno[3,2-*b*]pyrrolylidene]-5,5'-(4*H*,4'*H'*)-dione was synthesized according to the reported literature. ¹H NMR and ¹³C NMR spectra were recorded on an Agilent 400 MHz spectrometer using deuterated 1,1,2,2-tetrachloroethane (C₂Cl₄D₂) as solvent and tetramethylsilane (TMS) as an internal standard. Elementary analyses were carried out with a Flash 2000 element analyzer (Thermo Scientific, Netherlands) and MALDI-TOF MS spectra were collected using an Ultraflex III (Bruker, Germany). UV-Vis absorption spectra in solution and in thin films were measured using a UV-1800 (SHIMADZU) spectrophotometer. Cyclic voltammetry (CV) measurements were performed on AMETEK VersaSTAT 3 with a three-electrode cell system in a nitrogen bubbled 0.1 M tetra-*n*-butylammoniumhexafluorophosphate (*n*-Bu₄NPF₆) solution in dichloromethane at a scan rate of 100 mV/s at room temperature. Ag/Ag⁺ electrode, platinum wire, and platinum were used as the reference electrode, counter electrode, and working electrode, respectively. The Ag/Ag⁺ reference electrode was calibrated using a ferrocene/ferrocenium redox couple as an external standard, whose oxidation potential is set at -4.8 eV with respect to a zero vacuum level. The HOMO energy levels were obtained from the equation HOMO (eV) = -($E_{(ox)}^{onset} - E_{(ferrocene)}^{onset} + 4.8$). The LUMO levels were obtained from the equation LUMO (eV) = -($E_{(red)}^{onset} - E_{(ferrocene)}^{onset} + 4.8$). DFT calculations were performed using the Gaussian 09 package with the nonlocal hybrid Becke three-parameter Lee-Yang-Parr (B3LYP) function and the 6-31G

basis set to elucidate the HOMO and LUMO levels after optimizing the geometry of **TIIG-Bz**, **TIIG-Np**, and **TIIG-Bf** using the same method.

General Procedure for Suzuki Coupling and Small Molecule Purification

Dibrominated TIIG (0.457 mmol), phenylboronic acid, naphthalene-2-boronic acid pinacol ester, or benzo[*b*]furan-2-boronic acid (1.096 mmol), and tri(*o*-tolyl)phosphine (P(*o*-tolyl)₃, 45.6 μmol) were mixed with 15 mL of anhydrous toluene, and the mixture was degassed for 15 min. Potassium phosphate tribasic (K₃PO₄, 1.827 mmol) in 5 mL of water, 1 drop of aliquot 336, and tris(dibenzylideneacetone)dipalladium (0) (Pd₂(dba)₃, 11.3 μmol) were then added to the mixture and degassed again for 5 minutes. The reaction mixture was stirred vigorously at 90 °C for 48 h under argon atmosphere. After complete reaction, the mixture was put to room temperature. The crude product was then poured into 100 mL of toluene, washed three times with water, and once with brine. The combined organic layer was dried (MgSO₄) and concentrated *in vacuo*. Subsequently, the crude product was purified by column chromatography on silica gel with 0–70% chloroform in hexane as eluent. The solvent was evaporated under reduced pressure. The final solid was precipitated into methanol and filtered to afford a greenish blue solid.

Synthesis of TIIG-Bz

Isolated yield = 80%. ¹H NMR (400 MHz, C₂Cl₄D₂): δ (ppm) 7.74 (d, 4H, *J* = 7.6 Hz), 7.44 (t, 4H, *J* = 6.8 Hz), 7.37 (t, 2H, *J* = 7.6 Hz), 7.01 (s, 2H), 3.70 (d, 4H, *J* = 7.6 Hz), 1.87–1.90 (m, 2H), 1.32–1.46 (m, 16H), 0.89–0.97 (m, 12H). ¹³C NMR (400 MHz, C₂Cl₄D₂): *c* (ppm) 171.04, 152.29, 152.05, 134.23, 129.27, 128.90, 125.87, 120.07, 114.09, 107.64, 45.91, 38.57, 30.64, 28.72, 24.04, 23.26, 14.32, 10.89. MALDI-TOF MS (*m/z*) Calcd: 650.30. Found: 650.94 (MH⁺). Anal. Calcd. for C₄₀H₄₆N₂O₂S₂: C, 73.81; H, 7.12; N, 4.30; S, 9.85; O, 4.92. Found: C, 73.93; H, 6.97; N, 3.99; S, 9.86; O, 4.97.

Synthesis of TIIG-Np

Isolated yield = 78%. ¹H NMR (400 MHz, C₂Cl₄D₂): δ (ppm) 8.20 (s, 2H), 7.85–7.89 (m, 6H), 7.80–7.82 (m, 2H), 7.50–7.56 (m, 4H), 7.07 (s, 2H), 3.71 (d, 4H, *J* = 7.2 Hz), 1.89–1.91 (m, 2H), 1.33–1.50 (m, 16H), 0.91–0.99 (m, 12H). ¹³C NMR (400 MHz, C₂Cl₄D₂): δ (ppm) 171.06, 152.23, 152.10, 133.54, 133.27, 131.66, 128.91, 128.38, 127.96, 127.17, 126.87, 124.45, 123.82, 119.98, 114.38, 107.84, 45.96, 38.60, 30.66, 28.73, 24.08, 23.30, 14.36, 10.94. MALDI-TOF MS (*m/z*) Calcd: 750.33. Found: 751.05 (MH⁺). Anal. Calcd for C₄₈H₅₀N₂O₂S₂: C, 76.76; H, 6.71; N, 3.73; S, 8.54; O, 4.26. Found: C, 76.53; H, 6.54; N, 3.52; S, 8.67; O, 4.53.

Synthesis of TIIG-Bf

Isolated yield = 75.6%. ¹H NMR (400 MHz, C₂Cl₄D₂): δ (ppm) 7.59 (d, 2H, *J* = 7.6 Hz), 7.53 (d, 2H, *J* = 8 Hz), 7.35 (t, 2H, *J* = 6.8 Hz), 7.28 (t, 2H, *J* = 7.6 Hz), 7.08 (s, 2H), 7.05 (s, 2H), 3.71 (d, 4H, *J* = 7.6 Hz), 1.89–1.91 (m, 2H), 1.34–1.45 (m, 16H),

0.92–0.98 (m, 12H). ¹³C NMR (400 MHz, C₂Cl₄D₂): δ (ppm) 171.03, 154.85, 151.76, 151.22, 140.24, 129.05, 125.54, 123.74, 121.32, 119.82, 115.32, 111.31, 108.02, 103.53, 46.00, 38.53, 30.62, 28.70, 24.04, 23.27, 14.34, 10.87. MALDI-TOF MS (*m/z*) Calcd: 730.29. Found: 731.15 (MH⁺). Anal. Calcd for C₄₄H₄₆N₂O₄S₂: C, 72.30; H, 6.34; N, 3.83; S, 8.77; O, 8.76. Found: C, 72.59; H, 6.54; N, 3.79; S, 8.53; O, 8.74.

Fabrication and Characterization of OPVs

Indium tin oxide (ITO) coated glass substrates were scrubbed with detergent, then ultrasonicated in distilled water, acetone, and isopropyl alcohol for 10 min each and dried overnight in an oven at 100 °C. Poly(3,4-ethylene dioxythiophene:poly(styrenesulfonate) (PEDOT:PSS) (Baytron P VPAI 4083, H. C. Starck) was spin-coated on the ITO substrates at 5000 rpm for 40 s, then thermally annealed at 140 °C for 10 min in air. The samples were then transferred to a glove box. Small molecule:PC₆₁BM (blend ratios of 3:7, 4:6, 5:5, 6:4, and 7:3 (w/w) in chloroform were spin-coated from 1000 to 7000 rpm for 60 s on the top of the PEDOT:PSS/ITO coated substrates. Small molecule:PC₇₁BM solutions were prepared using optimal blend ratios (7:3, 6:4, and 6:4 (w/w) for **TIIG-Bz**, **TIIG-Np**, and **TIIG-Bf**, respectively), and deposited using the optimal spin rates identified using PC₆₁BM. Subsequently, Al electrodes (100 nm) were deposited by thermal evaporation under vacuum (<10⁻⁶ torr) yielding devices with an area of 13.0 mm². Completed devices were thermally annealed at 80 °C and 100 °C for 10 min using a digital hotplate. Current density–voltage (*J*–*V*) characteristics of OPVs were measured using a Keithley 2365A source measure unit. OPVs were characterized under simulated sun light (AM 1.5 G) with an intensity of 100 mW cm⁻² which was calibrated with a standard silicon photodiode (PV Measurements, Inc.). IPCE spectra were measured using a QEX7 quantum efficiency measurement system (PV Measurements, Inc.). For SCLC measurements, hole-only devices (ITO/PEDOT:PSS/**TIIG-Bz**, **TIIG-Np**, or **TIIG-Bf**:PC₇₁BM/Au) and electron-only devices (FTO/**TIIG-Bz**, **TIIG-Np**, or **TIIG-Bf**:PC₇₁BM/Al, FTO:fluorine-doped tin oxide) were fabricated, respectively. The samples were kept in a nitrogen atmosphere and thermally annealed at 100 °C. The mobilities using space charge limited current (SCLC) method were calculated by fitting the *J*–*V* characteristics of the single carrier diodes using the Mott-Gurney relationship, $J_{\text{sclc}} = (9/8) \times (\epsilon_r \epsilon_0 \mu) \times (V_a^2/L^3)$, where ϵ_r is the dielectric constant of the material, ϵ_0 is the permittivity of free space, μ is hole or electron mobility, *L* is the distance between the cathode which is equal to the film thickness, and *V_a* is the applied voltage. Film thickness was measured using a profilometer (ST4000-DLX, KMAC, Korea).

AFM and GIWAXS Measurements

Tapping-mode AFM images (1.5 μm × 1.5 μm) were obtained using a Multimode V microscope (Veeco, USA) with a nanoscope controller using silicon probes (Bruker) with a resonant frequency of 300 kHz. GIWAXS measurements were conducted at the PLS-II 9A U-SAXS beam line of Pohang

Accelerator Laboratory. X-ray light coming from the in-vacuum undulator (IVU) was monochromated ($E_k = 11.24$ keV, $\lambda = 1.103$ Å) using a Si (111) double crystal monochromator and focused horizontally and vertically at the sample position (450 (H) \times 60 (V) μm^2 in FWHM) using a K–B-type focusing mirror system. The GIWAXS sample stage was equipped with a 7-axis motorized stage for the fine alignment of the sample and the incidence angle of X-rays was adjusted to 0.12 – 0.14° . GIWAXS patterns were recorded by a 2D CCD detector (SX165, Rayonix, USA), and X-ray irradiation time was 0.5 – 5 s depending on the saturation level of the detector. The diffraction angle was calibrated with a sucrose standard (monoclinic, $P2_1$, $a = 10.8631$ Å, $b = 8.7044$ Å, $c = 7.7624$ Å, $\beta = 102.938^\circ$) and the sample-to-detector distance was approximately 232 mm. Samples for GIWAXS measurements were prepared by spin-coating of pristine small molecules and small molecule:PC₇₁BM blend solutions onto silicon wafers, with or without thermal annealing at 100 °C for 10 min.

Acknowledgements

This research was supported by New & Renewable Energy of the Korea Institute of Energy Technology Evaluation and Planning (KETEP) grant funded by the Korea government Ministry of Knowledge Economy (No. 20123010010140, 2012T100100740) and BK21 Plus (10Z20130011057), the National Research Foundation of Korea (2013R1A1A1A05004475, NRF-2013R1A1A2011591). Experiments at the PLS-II 9A U-SAXS beamline were supported, in part, by MEST and POSTECH.

Notes and references

Department of Energy Engineering, School of Energy and Chemical Engineering, Low Dimensional Carbon Materials Center, Ulsan National Institute of Science and Technology (UNIST), Ulsan 689-798, South Korea.

†Electronic Supplementary Information (ESI) available: Additional photovoltaic device performance, J – V characteristics, SCLC data, and GIWAXS packing parameters. See DOI: 10.1039/b000000x/

‡These authors contributed equally.

*E-mail: jykim@unist.ac.kr; yang@unist.ac.kr

1. B. C. Thompson and J. M. Fréchet, *Angew. Chem. Int. Ed.*, 2008, **47**, 58–77.
2. P.-L. T. Boudreault, A. Najari and M. Leclerc, *Chem. Mater.*, 2010, **23**, 456–469.
3. B. Walker, C. Kim and T.-Q. Nguyen, *Chem. Mater.*, 2010, **23**, 470–482.
4. Y.-J. Cheng, S.-H. Yang and C.-S. Hsu, *Chem. Rev.*, 2009, **109**, 5868–5923.
5. H.-Y. Chen, J. Hou, S. Zhang, Y. Liang, G. Yang, Y. Yang, L. Yu, Y. Wu and G. Li, *Nature Photon.*, 2009, **3**, 649–653.
6. Y. Li, *Acc. Chem. Res.*, 2012, **45**, 723–733.
7. S. Zhang, L. Ye, W. Zhao, B. Yang, Q. Wang and J. Hou, *Sci. China Chem.*, 2015, **58**, 248–256.
8. J.-D. Chen, C. Cui, Y.-Q. Li, L. Zhou, Q.-D. Ou, C. Li, Y. Li and J.-X. Tang, *Adv. Mater.*, 2015, **27**, 1035–1041.
9. Y. Liu, J. Zhao, Z. Li, C. Mu, W. Ma, H. Hu, K. Jiang, H. Lin, H. Ade and H. Yan, *Nat Commun*, 2014, **5**, DOI: 10.1038/ncomms6293.

10. H. Burckstummer, N. M. Kronenberg, M. Gsanger, M. Stolte, K. Meerholz and F. Wurthner, *J. Mater. Chem.*, 2010, **20**, 240–243.
11. J. Roncali, *Acc. Chem. Res.*, 2009, **42**, 1719–1730.
12. B. Walker, A. B. Tamayo, X.-D. Dang, P. Zalar, J. H. Seo, A. Garcia, M. Tantiwiwat and T.-Q. Nguyen, *Adv. Funct. Mater.*, 2009, **19**, 3063–3069.
13. O. P. Lee, A. T. Yiu, P. M. Beaujuge, C. H. Woo, T. W. Holcombe, J. E. Millstone, J. D. Douglas, M. S. Chen and J. M. Fréchet, *Adv. Mater.*, 2011, **23**, 5359–5363.
14. W. Li, K. H. Hendriks, A. Furlan, W. C. Roelofs, M. M. Wienk and R. A. Janssen, *J. Am. Chem. Soc.*, 2013, **135**, 18942–18948.
15. E. Wang, Z. Ma, Z. Zhang, K. Vandewal, P. Henriksson, O. Inganäs, F. Zhang and M. R. Andersson, *J. Am. Chem. Soc.*, 2011, **133**, 14244–14247.
16. A. R. Han, G. K. Dutta, J. Lee, H. R. Lee, S. M. Lee, H. Ahn, T. J. Shin, J. H. Oh and C. Yang, *Adv. Funct. Mater.*, 2015, **25**, 247–254.
17. G. Kim, S.-J. Kang, G. K. Dutta, Y.-K. Han, T. J. Shin, Y.-Y. Noh and C. Yang, *J. Am. Chem. Soc.*, 2014, **136**, 9477–9483.
18. K. C. Lee, W.-T. Park, Y.-Y. Noh and C. Yang, *ACS Appl. Mater. Interfaces*, 2014, **6**, 4872–4882.
19. R. S. Ashraf, A. J. Kronemeijer, D. I. James, H. Sirringhaus and I. McCulloch, *Chem. Commun.*, 2012, **48**, 3939–3941.
20. Y. Koizumi, M. Ide, A. Saeki, C. Vijayakumar, B. Balan, M. Kawamoto and S. Seki, *Polym. Chem.*, 2013, **4**, 484–494.
21. G. W. Van Pruissen, F. Gholamrezaie, M. M. Wienk and R. A. Janssen, *J. Mater. Chem.*, 2012, **22**, 20387–20393.
22. G. K. Dutta, A. Han, J. Lee, Y. Kim, J. H. Oh and C. Yang, *Adv. Funct. Mater.*, 2013, **23**, 5317–5325.
23. M. Ide, Y. Koizumi, A. Saeki, Y. Izumiya, H. Ohkita, S. Ito and S. Seki, *J. Phys. Chem. C*, 2013, **117**, 26859–26870.
24. M. S. Chen, J. R. Niskala, D. A. Unruh, C. K. Chu, O. P. Lee and J. M. Fréchet, *Chem. Mater.*, 2013, **25**, 4088–4096.
25. T. Odajima, M. Ashizawa, Y. Konosu, H. Matsumoto and T. Mori, *J. Mater. Chem. C*, 2014, **2**, 10455–10467.
26. S. Shen, P. Jiang, C. He, J. Zhang, P. Shen, Y. Zhang, Y. Yi, Z. Zhang, Z. Li and Y. Li, *Chem. Mater.*, 2013, **25**, 2274–2281.
27. A. Yassin, P. Leriche, M. Allain and J. Roncali, *New J. Chem.*, 2013, **37**, 502–507.
28. J. Mei, K. R. Graham, R. Stalder and J. R. Reynolds, *Org. Lett.*, 2010, **12**, 660–663.
29. J. C. Bijleveld, M. Shahid, J. Gilot, M. M. Wienk and R. A. J. Janssen, *Adv. Funct. Mater.*, 2009, **19**, 3262–3270.
30. V. Mihailetschi, J. Wildeman and P. Blom, *Phys. Rev. Lett.*, 2005, **94**, 126602.
31. J. Liu, B. Walker, A. Tamayo, Y. Zhang and T. Q. Nguyen, *Adv. Funct. Mater.*, 2013, **23**, 47–56.
32. B. Xue, B. Vaughan, C.-H. Poh, K. B. Burke, L. Thomsen, A. Stapleton, X. Zhou, G. W. Bryant, W. Belcher and P. C. Dastoor, *J. Phys. Chem. C*, 2010, **114**, 15797–15805.
33. V. S. Gevaerts, E. M. Herzig, M. Kirkus, K. H. Hendriks, M. M. Wienk, J. Perlich, P. Müller-Buschbaum and R. A. J. Janssen, *Chem. Mater.*, 2013, **26**, 916–926.

ARTICLE

Table of content

Thienoisindigo (TIIG)-Based Small Molecules